JOURNAL OF GUIDANCE, CONTROL, AND DYNAMICS
Vol. 24, No. 2, March–April 2001

Tight Formation Flight Control

Meir Pachter,* John J. D'Azzo,† and Andrew W. Proud‡
Air Force Institute of Technology, Wright–Patterson Air Force Base, Ohio 45433

The tight formation flight control problem is addressed. The formation consists of a lead and wing aircraft, where the wing flies in tight formation with the lead, such that the lead's trailing vortices aerodynamically couple the lead and the wing, and a reduction in the formation's induced drag is achieved. A controller (i.e., a formation-hold autopilot for the wing aircraft) is designed such that the formation's geometry is maintained in the face of lead aircraft maneuvers. In the formation flight control system, the wing and lead aircraft dynamics are coupled due to kinematic effects, and, in the case of tight formations, additional aerodynamic coupling effects are introduced. These additional aerodynamic coupling effects are properly modeled. The most significant aerodynamic coupling effect introduced by tight formation flight entails the coupling of the lateral/directional channel into the altitude-hold autopilot channel. It is shown that formation-hold autopilots designed ignoring the aerodynamic coupling effect yield satisfactory performance in tight formation flight.

Nomenclature

b	=	wingspan of wing
C_{L_L}	=	lift coefficient of the lead aircraft
S	=	surface area of wing
$\boldsymbol{V}_{\mathrm{SW}}$	=	sidewash
$\boldsymbol{W}$	=	wash vector
$\boldsymbol{W}_{\mathrm{UW}}$	=	upwash
$\bar{x}$	=	commanded longitudinal formation separation
$\bar{y}$	=	commanded lateral formation separation
y'	=	$\bar{y}/b$
$\bar{z}$	=	commanded vertical formation separation
z'	=	$\bar{z}/b$
Γ	=	lead vortex strength per unit length
ΔC_{D_W}	=	change in drag coefficient
ΔC_{L_W}	=	change in lift coefficient
ΔC_Y	=	change in side force coefficient
Δx	=	perturbation in longitudinal formation separation
Δy	=	perturbation in lateral formation separation
Δz	=	perturbation in vertical formation separation
μ	=	nondimensional correction factor
σ_{SW}	=	dimensionless change in induced sidewash
σ_{UW}	=	dimensionless change in induced drag

I. Introduction

THIS paper addresses the design of an autopilot for flying a wing aircraft in tight formation with the lead aircraft. The formation geometry is determined by the lead's $\bar{x}$, $\bar{y}$, and $\bar{z}$ position relative to the wing aircraft, in a rotating frame of reference attached to the wing as shown in Fig. 1. A controller (i.e., a formation-hold autopilot for the wing aircraft), is designed such that the formation's geometry is maintained in the face of lead aircraft maneuvers. A tight formation is one in which the lateral separation between aircraft is less than a wingspan. In this case, aerodynamic coupling is introduced into the formation's dynamics, above and beyond the kinematically induced coupling.

Thus, a lead aircraft moving through the air creates vortices behind the wing, as shown in Fig. 2. These vortices exert aerodynamic forces and moments on the wing aircraft in the formation.

By properly positioning the wing aircraft relative to the lead aircraft, the aerodynamic forces created by the lead's vortex can be used to reduce the fuel consumption of the wing aircraft. Indeed, the vortex shed by the lead aircraft induces an upwash on the wing aircraft's wing, which is responsible for reducing the wing's induced drag. The optimal spacing between the wing and lead aircraft, determined by aerodynamic calculations (when the nondimensional small correction factor μ is applied, the corrected optimal lateral position is $\bar{y} = b\sqrt{[(\pi/4)^2 + 3\mu^2]}$, is $\bar{y} = (\pi/4)b$ and $\bar{z} = 0$, where b is the wingspan of the lead aircraft. This is the optimal formation geometry that maximizes the reduction in the formation's induced drag. To fully take advantage of the reduction in induced drag afforded by tight formations, the wing's perturbations in position relative to the lead must stay within 10% of the lead's wingspan. Thus, alternating aircraft in and out of the lead position can potentially increase the range and endurance of a formation of aircraft by 30% (Ref. 1).

In previous work, the formation flight control problem was introduced and attention was given to the kinematic coupling and autopilot saturation effects (see, for example, Refs. 2–9). In this paper the additional aerodynamic coupling effects introduced by tight formation flight are properly modeled and a formation-hold autopilot for tight formation is designed. In Secs. II and III the aerodynamic effects in tight formation flight are modeled. The upwash created by flying the wing in the lead's vortex is calculated and in Sec. IV the developed theory is applied to the modeling of a tight formation flight control system (FFCS) for an F-16 class aircraft. The kinematic coupling effects that apply to both large and tight formations are modeled in Sec. V, and the complete tight formation flight control system is developed in Sec. VI. The formation-hold autopilot is designed in Sec. VII, and the resulting performance is evaluated in Sec. VIII using a simulation developed in MATLAB® SIMULINK, which includes the nonlinear kinematic effects. Formation heading change maneuvers are simulated. A comparison of results with and without the aerodynamic coupling effects caused by a tight formation included is also presented. Finally, in Sec. IX, conclusions are drawn.

II. Upwash and Sidewash Modeling

A. Biot–Savart

This section outlines the method used to calculate the upwash and sidewash created by the lead aircraft on the wing aircraft. The derivation of the effect of the lead aircraft's wing vortex on the wingman's wing is determined by using an analogy with electric field strength produced by an electric current in electromagnetics. A vortex filament from Fig. 2 is redrawn in Fig. 3. The angles β_1 and β_2 determined by the vortex filament segment $[A' \;\; B']$ and the point P, are shown in Fig. 3. The fluid dynamics analogue of the Biot–Savart law from electromagnetics states that the induced velocity $\boldsymbol{W}$ from vortex filament A is given by

$$\boldsymbol{W} = (\hat{\boldsymbol{\Phi}}\Gamma/4\pi\boldsymbol{r}_c)(\cos\beta_1 - \cos\beta_2) \tag{1}$$

Received 28 May 1999; revision received 29 February 2000; accepted for publication 14 April 2000. This paper is declared a work of the U.S. Government and is not subject to copyright protection in the United States.

*Professor, Electrical Engineering Department.
†Professor Emeritus, Electrical Engineering Department.
‡Captain, U.S. Air Force Research Laboratory.

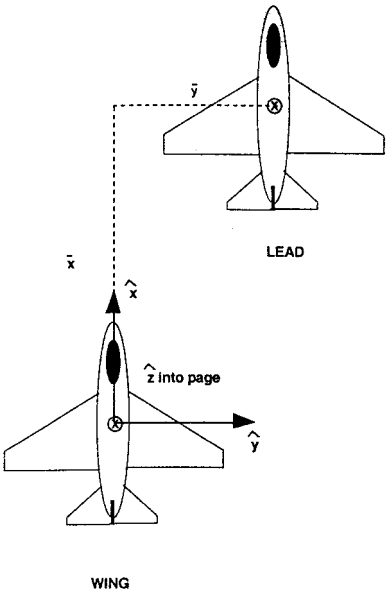

Fig. 1 Formation geometry.

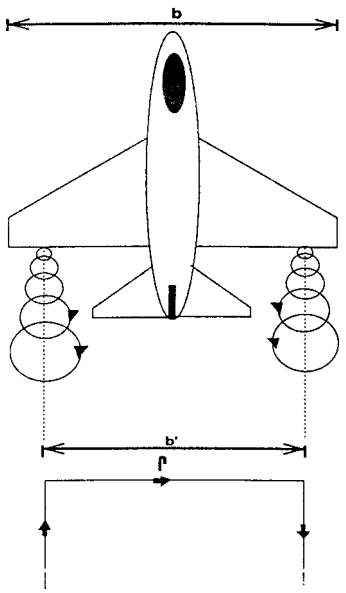

Fig. 2 Horseshoe vortex.

where $\boldsymbol{r}_c$ is the distance from the vortex filament to the point P, and the velocity of the air wash caused by the vortex filament at point P and out of the page is $\boldsymbol{W}$. The unit vector $\hat{\boldsymbol{\Phi}}$ is orthogonal to the radius vector $\boldsymbol{r}_c$. When point A' is at $-\infty$, the angle $\beta_1 = 0$, and when point B' is at $+\infty$, the angle $\beta_2 = \pi$. Assuming that the longitudinal separation in the formation is large, that is, greater than two wingspans, is tantamount to saying that point B' is effectively at $+\infty$. When the actual distance between the tail of the leader and the nose of the wing is greater than $2b$, this effectively places point B' at $+\infty$. Then the lead aircraft's spanwise contribution to the flowfield near the wing aircraft can be neglected. Similarly, the wing aircraft's influence on the flowfield near the lead aircraft's wing can be neglected. These are the main assumptions used here for the location of the wing aircraft's wing with respect to the vortices caused by the lead aircraft's wing. The vortex goes back a great distance before it is diffused, and the assumption that point A' is essentially at $-\infty$ is validated. This reduces Eq. (1) to the simplified form of the Biot–Savart law,

$$\boldsymbol{W} = \hat{\boldsymbol{\Phi}}\Gamma/2\pi\boldsymbol{r}_c \tag{2}$$

The wash vector $\boldsymbol{W}$ at the point P for the geometry of Fig. 3 is out of the page. This would be the special case of no sidewash and all upwash at point P on the page.

Figure 4 is a view from above the two aircraft that contains both the lead aircraft replaced by its horseshoe vortex approximation,

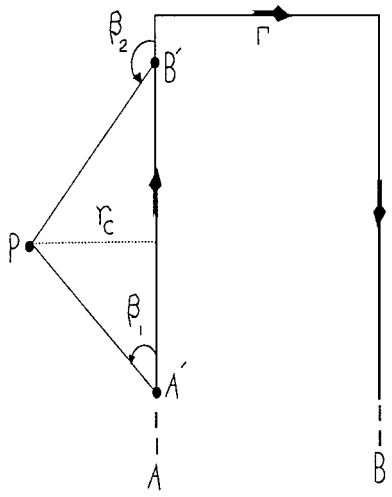

Fig. 3 Field strength at point P due to filament A.

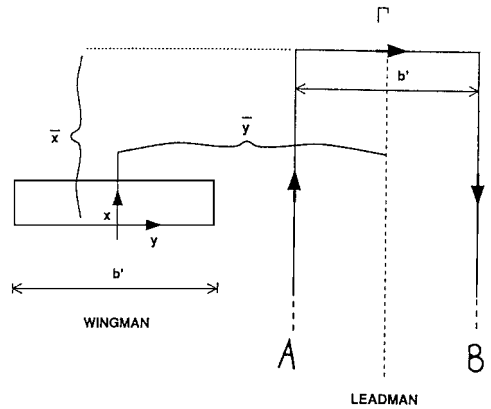

Fig. 4 View from above the two aircraft.

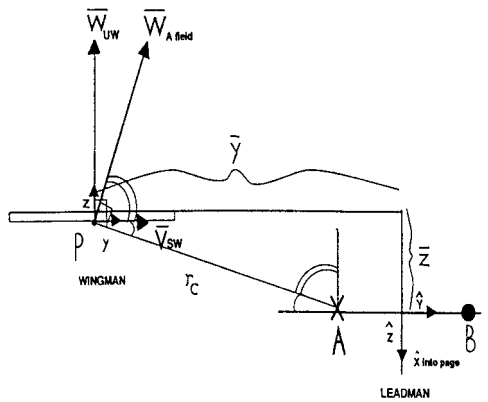

Fig. 5 Behind view showing W_A field.

with the sides of the horseshoe represented by the A and B filaments. The wing aircraft is represented by its elliptical wing approximation. The reduced wingspan of the wing aircraft is represented by b'. This is the corrected value for an elliptical lift distribution on a wing:

$$b' = (\pi/4)b \tag{3}$$

Figure 5 shows the view from behind the two aircraft. The radius vectors $\boldsymbol{r}_c$ from each vortex filament to the wing, disregarding the $\hat{x}$ component due to the effectively infinite length of the filaments, are for filaments A and B

$$\boldsymbol{r}_A = [\bar{y} - (b'/2) - y]\hat{\boldsymbol{y}} + (\bar{z} - z)\hat{\boldsymbol{z}} \tag{4}$$

$$\boldsymbol{r}_B = [\bar{y} + (b'/2) - y]\hat{\boldsymbol{y}} + (\bar{z} - z)\hat{\boldsymbol{z}} \tag{5}$$

where, $\hat{\boldsymbol{y}}$ and $\hat{\boldsymbol{z}}$ are the unit directional vectors. Based on Fig. 5 and with a bit of geometrical insight, it can be shown that the total

upwash $\boldsymbol{W}_{\mathrm{UW}}$ at station $(y, 0)$ from both filaments emanating from the lead's wing is

$$\boldsymbol{W}_{\mathrm{UW}} = -\frac{\Gamma_L}{2\pi}\left\{\frac{[\bar{y}-(b'/2)-y]}{[\bar{y}-(b'/2)-y]^2+\bar{z}^2} - \frac{[\bar{y}+(b'/2)-y]}{[\bar{y}+(b'/2)-y]^2+\bar{z}^2}\right\} \qquad -\frac{1}{2}b' \le y \le \frac{1}{2}b' \quad (6)$$

The total induced sidewash $\boldsymbol{V}_{\mathrm{SW}}$ at station $(0, z)$ from both filaments is

$$\boldsymbol{V}_{\mathrm{SW}} = \frac{\Gamma_L}{2\pi}\left\{\frac{(\bar{z}-z)^2}{[\bar{y}-(b'/2)]^2+(\bar{z}-z)^2} - \frac{(\bar{z}-z)^2}{[\bar{y}+(b'/2)]^2+(\bar{z}-z)^2}\right\} \qquad 0 \ge z \ge -h_z \quad (7)$$

B. Average Upwash and Sidewash

The average induced upwash on the wing aircraft's wing is, thus, calculated by integrating Eq. (6):

$$\boldsymbol{W}_{\mathrm{UW_{avg}}} = -\frac{\Gamma_L}{2\pi b}\int_{-b'/2}^{b'/2}\left\{\frac{[\bar{y}-(b'/2)-y]}{[\bar{y}-(b'/2)-y]^2+\bar{z}^2} - \frac{[\bar{y}+(b'/2)-y]}{[\bar{y}+(b'/2)-y]^2+\bar{z}^2}\right\}\mathrm{d}y \quad (8)$$

After changing the variables to $u = \{[\bar{y}-(b'/2)-y]^2+\bar{z}^2\}$ for the first term and similarly $u' = \{[\bar{y}+(b'/2)-y]^2+\bar{z}^2\}$ for the second term, and changing the limits to match with the new variables u and u', the integral in Eq. (8) is evaluated as

$$\boldsymbol{W}_{\mathrm{UW_{avg}}} = -\frac{\Gamma_L}{4\pi b'}\left[\ell n\frac{\bar{y}^2+\bar{z}^2}{(\bar{y}-b')^2+\bar{z}^2} - \ell n\frac{(\bar{y}+b')^2+\bar{z}^2}{\bar{y}^2+\bar{z}^2}\right] \quad (9)$$

Similarly, averaging by integrating from the bottom of the tail at 0 to the top of the tail at $-h_z$ yields the average sidewash at the vertical tail

$$\boldsymbol{V}_{\mathrm{SW_{avg}}} = \frac{\Gamma_L}{4\pi h_z}\left\{\ell n\frac{[\bar{y}-(b'/2)]^2+\bar{z}^2}{[\bar{y}-(b'/2)]^2+(\bar{z}+h_z)^2} - \ell n\frac{[\bar{y}+(b'/2)]^2+\bar{z}^2}{[\bar{y}^2+(b'/2)]+(\bar{z}+h_z)^2}\right\} \quad (10)$$

C. Corrected Average Upwash and Sidewash

In this paper, the horseshoe approximation of the vortex shed from the lead airdcraft's wing is employed. A correction term μ^2 needs to be included in both the numerator and denominator of each term contained in the natural logarithms in Eqs. (9) and (10) to take into account physical viscosity effects and to make the mathematical derivation more accurately follow the experimental data.[1] This is a dimensionless number and requires both the numerator and denominator terms inside the logarithm to be nondimensionalized. To make the terms nondimensional, both the numerators and denominators are divided by b^2. The correction term μ^2 is then added to both numerators and denominators. The resulting equations are

$$\boldsymbol{W}_{\mathrm{UW_{avg}}} = -\frac{\Gamma_L}{4\pi b}\left\{\ell n\frac{y'^2+z'^2+\mu^2}{[y'-(\pi/4)]^2+z'^2+\mu^2} - \ell n\frac{[y'+(\pi/4)]^2+z'^2+\mu^2}{y'^2+z'^2+\mu^2}\right\} \quad (11)$$

$$\boldsymbol{V}_{\mathrm{SW_{avg}}} = \frac{\Gamma_L}{4\pi h_z}\left\{\ell n\frac{[y'-(\pi/8)]^2+z'^2+\mu^2}{[y'-(\pi/8)]^2+[z'+(h_z/b)]^2+\mu^2} - \ell n\frac{[y'+(\pi/8)]^2+z'^2+\mu^2}{[y'+(\pi/8)]^2+[z'+(h_z/b)]^2+\mu^2}\right\} \quad (12)$$

where now the nondimensional formation geometry parameters are $y' = \bar{y}/b$ and $z' = \bar{z}/b$.

III. Calculation of Change in Lift and Drag

The upwash on the wing causes a change in the angle of attack of the wing. This causes a rotation in the lift and drag vectors.

A. Change in Drag

In Fig. 6, V is the velocity of the aircraft, W is the upwash, and V' is the composite velocity of the air at the surface of the wing. The original lift and drag vectors are represented by $\boldsymbol{L}$ and $\boldsymbol{D}$ and the rotated lift and drag are represented by L' and D', respectively. It can be seen from Fig. 6 that the change in angle of attack is

$$\Delta\alpha = \arctan(|\boldsymbol{W}_{\mathrm{UW}}|/V) \approx |\boldsymbol{W}_{\mathrm{UW}}|/V \quad (13)$$

where the approximation for small angles has been applied. It can also be seen from Fig. 6 that consequently the change in drag due to the rotation of the lift vector is

$$\Delta\boldsymbol{D}_W = -\boldsymbol{L}_W \tan\Delta\alpha \approx -\boldsymbol{L}_W(|\boldsymbol{W}_{\mathrm{UW}}|/V) \quad (14)$$

where again, the small-angle approximation is used. Dividing both sides by the dynamic pressure $\bar{q}$ and the surface area S of the wing, the nondimensional coefficient of drag increment is

$$\Delta C_{D_W} = (\Delta\boldsymbol{D}_W/\bar{q}S) = -(\boldsymbol{L}_W/\bar{q}S)(|\boldsymbol{W}_W|/V) = -C_{L_W}(\boldsymbol{W}_W/V) \quad (15)$$

Also, the vortex strength per unit length can be expressed as

$$\Gamma = \frac{\boldsymbol{L}_L}{\rho V b'} = \frac{\boldsymbol{L}_L}{\rho V(\pi/4)b} = \frac{\frac{1}{2}\rho V^2 S C_{L_L}}{\rho V(\pi/4)b} = \frac{2}{\pi}\frac{S}{b^2}C_{L_L}Vb = \frac{2}{\pi\mathcal{AR}}C_{L_L}Vb \quad (16)$$

where S is the area of wing, V is the airspeed of formation, $\mathcal{AR}$ is the aspect ratio of wing, and C_{L_L} is the lift coefficient of the lead aircraft. Substituting the preceding equation for vortex strength and also substituting the earlier derived upwash expression into the change in drag equation yields

$$\Delta C_{D_W} = \frac{1}{\pi\mathcal{AR}}C_{L_L}C_{L_W}\frac{2}{\pi^2}\left\{\ell n\frac{y'^2+z'^2+\mu^2}{[y'-(\pi/4)]^2+z'^2+\mu^2} - \ell n\frac{[y'+(\pi/4)]^2+z'^2+\mu^2}{y'^2+z'^2+\mu^2}\right\} \quad (17)$$

B. Change in Lift

The change in lift coefficient is given by

$$\Delta C_{L_W} = \Delta\alpha a_W = (|\boldsymbol{W}_{\mathrm{UW}}|/V)a_W \quad (18)$$

where a_W is the lift curve slope of the wing. Substitution of the upwash and vortex strength values, as before, results in

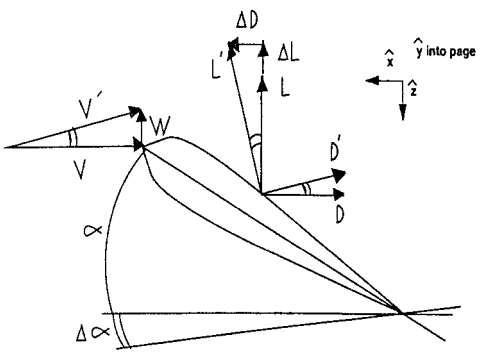

Fig. 6 Side view of wingman's wing lift rotation.

$$\Delta C_{L_W} = \frac{a_W}{\pi \mathcal{AR}} C_{L_L} \frac{2}{\pi^2} \left\{ \ell n \frac{y'^2 + z'^2 + \mu^2}{[y' - (\pi/4)]^2 + z'^2 + \mu^2} - \ell n \frac{[y' + (\pi/4)]^2 + z'^2 + \mu^2}{y'^2 + z'^2 + \mu^2} \right\} \tag{19}$$

This is the change in lift coefficient of the wing from the upwash created by the lead aircraft.

C. Change in Side Force

The sidewash created by the lead also causes a change in the force on the vertical tail. This change in side force is

$$\Delta \boldsymbol{F}_Y = \eta \bar{q} S_{\text{vt}} a_{\text{vt}} (|\boldsymbol{V}_{\text{SW}}| / V) \tag{20}$$

where η is the aerodynamic efficiency factor at the tail, S_{vt} is the vertical tail area, and a_{vt} is the lift curve slope of the vertical tail. The nondimensional change in side force coefficient is

$$\Delta C_Y = \eta (S_{\text{vt}}/S) a_{\text{vt}} (|\boldsymbol{V}_{\text{SW}}| / V) \tag{21}$$

Inserting the sidewash expression of Eq. (12) back into the nondimensional side force Eq. (21) gives the side force coefficient

$$\Delta C_Y = \eta \frac{S_{\text{vt}}}{S} \frac{a_{\text{vt}}}{V} \frac{\Gamma_L}{4\pi h_z} \left\{ \ell n \frac{[y' - (\pi/8)]^2 + z'^2 + \mu^2}{[y' - (\pi/8)]^2 + [z' + (h_z/b)]^2 + \mu^2} - \ell n \frac{[y' + (\pi/8)]^2 + z'^2 + \mu^2}{[y' + (\pi/8)]^2 + [z' + (h_z/b)]^2 + \mu^2} \right\} \tag{22}$$

Finally, substituting for Γ by using Eq. (16), the change in side force coefficient becomes

$$\Delta C_Y = \frac{1}{\pi \mathcal{AR}} \frac{\eta S_{\text{vt}} a_{\text{vt}} C_{L_L} b}{2 S h_z} \frac{2}{\pi} \times \left\{ \ell n \frac{[y' - (\pi/8)]^2 + z'^2 + \mu^2}{[y' - (\pi/8)]^2 + [z' + (h_z/b)]^2 + \mu^2} - \ell n \frac{[y' + (\pi/8)]^2 + z'^2 + \mu^2}{[y' + (\pi/8)]^2 + [z' + (h_z/b)]^2 + \mu^2} \right\} \tag{23}$$

IV. Modified Wing Aircraft Control System

It is envisaged that each aircraft is equipped with a flight control system that includes three standard autopilots: heading-hold, Mach-hold, and altitude-hold autopilots. The aircraft/autopilot models are low-order models: the Mach-hold and the heading-hold autopilots are first order, and the altitude-hold autopilot is second order. The conventional models for the aircraft/autopilots dynamical systems are based on an individual aircraft in undisturbed air. These aircraft/autopilot models were developed in Ref. 4, using the principles presented in Ref. 10. They make up the basic flight control system (FCS) for the lead and wing aircraft.

The formation flight control autopilot resides on the wing aircraft. It is an outer-loop controller that receives measurements of the lead aircraft's position relative to the wing aircraft, and it drives the reference signals of the wing's three axes (Mach-hold, heading-hold, and altitude-hold) autopilots.

For tight formation flight, the wing FCS needs to be modified to account for the additional aerodynamic interactions created by the upwash and sidewash from the lead aircraft. The upwash causes an aerodynamic force in the $\hat{x}$ and $\hat{z}$ directions in the form of a change in drag and change in lift as derived earlier. Thus, the wing aircraft needs to be retrimmed in pitch. The sidewash induces a force in the $\hat{y}$ direction caused by a change in lift on the vertical tail, which requires the wing aircraft's lateral directional control channel to be retrimmed. This change in forces needs to be trimmed out by the wing's FCS. Above and beyond this retrimming action, it is important to include the dynamical change in forces caused by a perturbation Δx, Δy, and Δz in the lead's position in the formation relative to the wing.

The upwash and sidewash also cause changes in moments applied to the wing aircraft. However, consistent with the design philosophy adopted herein, moment effects are not explored in this paper. Thus, the formation-hold autopilot designed in this paper is an outer-loop controller that commands the wing aircraft's altitude, velocity, and heading. The latter are the reference signals for the respective inner-loop conventional autopilots and stability augmentation systems. This is why, in this paper, attention is confined to the wake-induced aerodynamic forces only. Thus, the moments applied to the wing aircraft and induced by the lead aircraft's wake are not modeled and are not incorportated into the design of the outer-loop formation-hold autopilot. Indeed, the main benefit of tight formation flight is afforded by the dominant effect of induced drag reduction. However, the rolling moment applied to the wing aircraft has to be trimmed out. The rejection of the rolling moment disturbances, caused by perturbations in the wake-induced rolling moment resulting from an instantaneous change in the lead's position relative to the wing, is relegated to the wing's inner-loop stability augmentation system, according to the design philosophy of the formation-hold autopilot and as described in the paper. Thus, in the formation flight mode the inner control loop might have to be tighter than would normally be required in free flight. This decomposition approach permits the use of the rather simplified modeling employed, where the wing aircraft is considered a point mass.

Thus, new stability derivatives for change in wing drag resulting from a change in the $\bar{x}$, $\bar{y}$, and $\bar{z}$ positions in the formation need to be determined for the Mach-hold channel. Similarly, the new stability derivatives for the change in lift due to a change in the $\bar{x}$, $\bar{y}$, and $\bar{z}$ positions need to be determined for the altitude-hold channel. Finally, new stability derivatives for the change in side force due to a change in the $\bar{x}$, $\bar{y}$, and $\bar{z}$ positions in the formation need to be determined for use in the heading-hold channel. The resulting wing aircraft/autopliot model for tight formation flight is

$$\dot{V}_W = -(1/\tau_V) V_W + (1/\tau_V) V_{W_c} + (\bar{q} S/m)\left[\Delta C_{D_{W_x}} x + \Delta C_{D_{W_y}} y + \Delta C_{D_{W_z}} z\right]$$

$$\dot{\psi}_W = -(1/\tau_\psi)\psi_W + (1/\tau_\psi)\psi_{W_c} + (\bar{q} S/mV)\left[\Delta C_{Y_{W_x}} x + \Delta C_{Y_{W_y}} y + \Delta C_{Y_{W_z}} z\right]$$

$$\ddot{h}_W = -\left[\left(1/\tau_{h_a}\right) + \left(1/\tau_{h_b}\right)\right]\dot{h}_W - \left(1/\tau_{h_a}\tau_{h_b}\right) h_W + \left(1/\tau_{h_a}\right) h_{W_c} + (\bar{q} S/m)\left[\Delta C_{L_{W_x}} x + \Delta C_{L_{W_y}} y + \Delta C_{L_{W_z}} z\right]$$

where V_{W_c} is the reference signal to the wing Mach-hold autopilot. Similarly, h_{W_c} is the reference signal to the altitude-hold autopilot, and ψ_{W_c} is the reference signal to the heading-hold autopilot. V_W is the wing's velocity, ψ_W is the wing's heading, h_W is the wing's altitude, and x, y, and z are the perturbations in the lead's position in the formation relative to the wing from the nominal location $(\bar{x}, \bar{y}, \bar{z})$. In the $\dot{V}_W$ differential equation the new stability derivatives for the longitudinal and the vertical perturbations, $\Delta C_{D_{W_x}}$, $\Delta C_{D_{W_y}}$, and $\Delta C_{D_{W_z}}$ and $\Delta C_{L_{W_x}}$, $\Delta C_{L_{W_y}}$, and $\Delta C_{L_{W_z}}$, respectively, are multiplied by $\bar{q} S/m$. Multiplying them by $\bar{q} S$ converts them into a force, and then dividing by the mass converts them to an acceleration, as required. The new stability derivatives for the heading differential equation are multiplied by $\bar{q} S/mV$. The additional division by the velocity is required because the heading rate is an angular velocity. Also, the centrifugal acceleration is $A = \omega \times V$ where V is the aircraft's velocity and ω is the angular velocity. Because ω and V are orthogonal, $\omega = A/V$. Hence, the new stability derivatives in the heading equation, when multiplied by $\bar{q} S/mV$, are converted to an angular velocity, as required in the heading equation.

A. New Formation Stability Derivatives

The change in drag, lift, and side force on the wing aircraft in a tight formation have been calculated earlier. To determine the change in these forces due to a change in the lead's x, y, and z relative position in the formation, a linearization[10] is performed about the nominal lead position (which is measured with respect to the wing's position) in the optimal tight formation: The latter is $\bar{y} = (\pi/4)b$ [or, more accurately, $\bar{y} = b\sqrt{[(\pi/4)^2 + 3\mu^2]}$ and $\bar{z} = 0$.

This requires that derivatives of the change in drag, lift, and side force be evaluated at these values for $\bar{y}$ and $\bar{z}$.

First, a dimensionless expression is introduced for the change in induced drag:

$$\sigma_{\mathrm{UW}}(y', z') = \frac{2}{\pi^2}\left\{ \ell n \frac{y'^2 + z'^2 + \mu^2}{[y' - (\pi/4)]^2 + z'^2 + \mu^2} - \ell n \frac{[y' + (\pi/4)]^2 + z'^2 + \mu^2}{y'^2 + z'^2 + \mu^2} \right\} \tag{24}$$

A similar nondimensional function is defined for the sidewash component:

$$\sigma_{\mathrm{SW}}(y', z') = \frac{2}{\pi}\left\{ \ell n \frac{[y' - (\pi/8)]^2 + z'^2 + \mu^2}{[y' - (\pi/8)]^2 + [z' + (h_z/b)]^2 + \mu^2} - \ell n \frac{[y' + (\pi/8)]^2 + z'^2 + \mu^2}{[y' + (\pi/8)]^2 + [z' + (h_z/b)]^2 + \mu^2} \right\} \tag{25}$$

Based on these definitions, the changes in lift, drag, and side force given in Eqs. (17), (18), and (21) are expressed as

$$\Delta C_{D_W} = (1/\pi A\mathbf{R}) C_{L_L} C_{L_W} \sigma_{\mathrm{UW}}(y', z') \tag{26}$$

$$\Delta C_{L_W} = (1/\pi A\mathbf{R}) a C_{L_W} \sigma_{\mathrm{UW}}(y', z') \tag{27}$$

$$\Delta C_{Y_W} = \frac{1}{\pi A\mathbf{R}} \frac{\eta S_{\mathrm{vt}} a_{\mathrm{vt}} b}{2 S h_z} C_{L_L} \sigma_{\mathrm{SW}}(y', z') \tag{28}$$

The only expressions in the preceding equations that vary with a change in the x, y, and z positions in the formation are the $\sigma_{\mathrm{UW}}(y', z')$ function for the change in drag and lift and the $\sigma_{\mathrm{SW}}(y', z')$ function for the change in side force. The derivatives of $\sigma_{\mathrm{UW}}(y', z')$ and $\sigma_{\mathrm{SW}}(y', z')$ are analytically obtained as follows: The partial derivatives for $\sigma_{\mathrm{UW}}(y', z')$ are calculated as

$$\left.\frac{\partial \sigma_{\mathrm{UW}}}{\partial x'}\right|_{y' = \pi/4, z' = 0} = 0 \tag{29}$$

$$\left.\frac{\partial \sigma_{\mathrm{UW}}}{\partial y'}\right|_{y' = \pi/4, z' = 0} = \frac{(3/8)\pi}{[(\pi/4)^2 + \mu^2][(\pi/2)^2 + \mu^2]} \tag{30}$$

$$\left.\frac{\partial \sigma_{\mathrm{UW}}}{\partial z'}\right|_{y' = \pi/4, z' = 0} = 0 \tag{31}$$

and the partial derivatives for $\sigma_{\mathrm{SW}}(y', z')$ are calculated as

$$\left.\frac{\partial \sigma_{\mathrm{SW}}}{\partial x'}\right|_{y' = \pi/4, z' = 0} = 0 \tag{32}$$

$$\left.\frac{\partial \sigma_{\mathrm{SW}}}{\partial y'}\right|_{y' = \pi/4, z' = 0} = \frac{\frac{1}{2}(h_z/b)^2}{[(\pi/8)^2 + \mu^2]\left[(\pi/8)^2 + (h_z/b)^2 + \mu^2\right]} - \frac{\frac{3}{2}(h_z/b)^2}{[(3\pi/8)^2 + \mu^2]\left[(3\pi/8)^2 + (h_z/b)^2 + \mu^2\right]} \tag{33}$$

$$\left.\frac{\partial \sigma_{\mathrm{SW}}}{\partial z'}\right|_{y' = \pi/4, z' = 0} = \frac{-(\pi/2)(h_z/b)}{\left[(\pi/8)^2 + \mu^2 + (h_z/b)^2\right]\left[(3\pi/8)^2 + \mu^2 + (h_z/b)^2\right]} \tag{34}$$

Inserting the preceding derivatives into the changes in the expressions for the drag, lift, and side force coefficients yields

$$\Delta C_{D_{Wx}} = \Delta C_{L_{Wx}} = \Delta C_{Y_{Wx}} = \Delta C_{D_{Wz}} = \Delta C_{L_{Wz}} = 0$$

$$\Delta C_{D_{Wy}} = \frac{1}{\pi A\mathbf{R}} C_{L_W}^2 \frac{\frac{3}{8}\pi}{[(\pi/4)^2 + \mu^2][(\pi/2)^2 + \mu^2]} \tag{35}$$

$$\Delta C_{L_{Wy}} = \frac{1}{\pi A\mathbf{R}} a C_{L_W} \frac{\frac{3}{8}\pi}{[(\pi/4)^2 + \mu^2][(\pi/2)^2 + \mu^2]} \tag{36}$$

$$\Delta C_{Y_{Wy}} = \frac{1}{\pi A\mathbf{R}} \frac{\eta S_{\mathrm{vt}} a_{\mathrm{vt}} h_z}{4 S b} C_{L_L} \times \left\{ \frac{1}{[(\pi/8)^2 + \mu^2]\left[(\pi/8)^2 + (h_z/b)^2 + \mu^2\right]} - \frac{3}{[(3\pi/8)^2 + \mu^2]\left[(3\pi/8)^2 + (h_z/b)^2 + \mu^2\right]} \right\} \tag{37}$$

$$\Delta C_{Y_{Wz}} = -\frac{1}{\pi A\mathbf{R}} \frac{\eta S_{\mathrm{vt}} a_{\mathrm{vt}}}{2S} C_{L_L} \times \frac{(\pi/2)(h_z/b)}{\left[(\pi/8)^2 + \mu^2 + (h_z/b)^2\right]\left[(3\pi/8)^2 + \mu^2 + (h_z/b)^2\right]} \tag{38}$$

B. Modified Wing Aircraft Control System

By the use of the stability derivatives just derived that are associated with the forces created by the upwash and sidewash, the new wing aicraft/autopilot dynamic system is

$$\dot{V}_W = -(1/\tau_V) V_W + (1/\tau_V) V_{W_c} + (\bar{q} S/m) \Delta C_{D_{W_y}} y \tag{39}$$

$$\dot{\psi}_W = -(1/\tau_{\psi W}) \psi_W + (1/\tau_{\psi W}) \psi_{W_c} + (\bar{q} S/m V)\left[\Delta C_{Y_{W_y}} y + \Delta C_{Y_{W_z}} z\right] \tag{40}$$

$$\ddot{h}_W = -\left[\left(1/\tau_{h_a}\right) + \left(1/\tau_{h_b}\right)\right] \dot{h}_W - \left(1/\tau_{h_a}\tau_{h_b}\right) h_W + \left(1/\tau_{h_a}\tau_{h_b}\right) h_{W_c} + (\bar{q} S/m) \Delta C_{L_{W_y}} y \tag{41}$$

where $\Delta C_{D_{W_y}}$, $\Delta C_{L_{W_y}}$, $\Delta C_{Y_{W_y}}$, and $\Delta C_{Y_{W_z}}$ are the new tight formation stability derivatives.

V. Formation Kinematics

The kinematic equations relating the separation between the lead and wing aircraft are developed in Refs. 3 and 4. A rotating reference frame affixed to the wing's instantaneous position and aligned with the wing's velocity vector is used, as shown in Fig. 7. The lead's position in the rotating reference frame is (x, y, z). The kinematic equations developed in Refs. 3 and 4 are

$$\frac{\mathrm{d}x}{\mathrm{d}t} = V_L \cos \psi_E + \dot{\psi}_W y - V_W \tag{42}$$

$$\frac{\mathrm{d}y}{\mathrm{d}t} = V_L \sin \psi_E + \dot{\psi}_W x \tag{43}$$

where the heading errror $\psi_E = \psi_L - \psi_W$.

VI. Complete System Model

Equations (39–41) are adjoined to the nonlinear kinematic Eqs. (42) and (43), where Eq. (40) for $\dot{\psi}$ is inserted into the x and y separation differential equations, yielding the novel six-dimensional tight formation control system:

$$\dot{x} = -(y/\tau_{\psi W}) \psi_W - V_W + V_L \cos(\psi_L - \psi_W) + (y/\tau_{\psi W}) \psi_{W_c} + y(\bar{q} S/m V_W)\left[\Delta C_{Y_{W_y}} (y - \bar{y}) + \Delta C_{Y_{W_z}} (z - \bar{z})\right] \tag{44}$$

$$\dot{y} = (x/\tau_{\psi W}) \psi_W + V_L \sin(\psi_L - \psi_W) - (x/\tau_{\psi W}) \psi_{W_c} - x(\bar{q} S/m V_W)\left[\Delta C_{Y_{W_y}} (y - \bar{y}) + \Delta C_{Y_{W_z}} (z - \bar{z})\right] \tag{45}$$

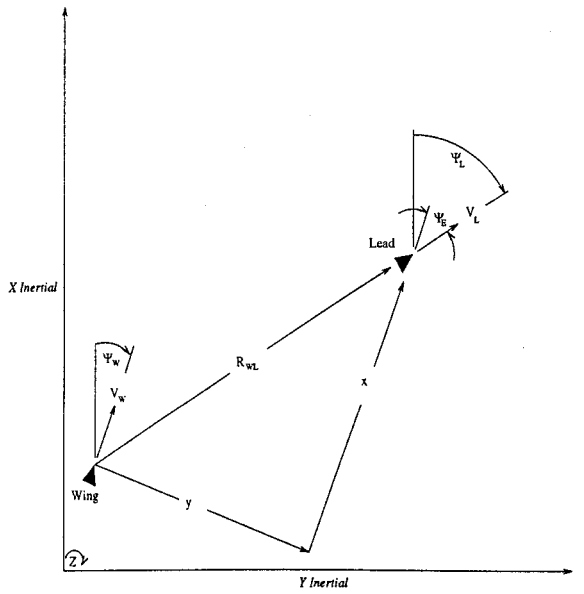

Fig. 7 Wing aircraft rotating reference frame.

$$\dot{V}_W = -(1/\tau_V)V_W + (1/\tau_V)V_{W_c} + (\bar{q}S/m)\Delta C_{D_{W_y}}(y - \bar{y}) \tag{46}$$

$$\dot{\psi}_W = (1/\tau_{\psi_W})\psi_W + (1/\tau_{\psi_W})\psi_{W_c} + (\bar{q}S/mV)\left[\Delta C_{Y_{W_y}}(y - \bar{y}) + \Delta C_{Y_{W_z}}(z - \bar{z})\right] \tag{47}$$

$$\dot{z} = \zeta \tag{48}$$

$$\dot{\zeta} = -\left[\left(1/\tau_{h_a}\right) + \left(1/\tau_{h_b}\right)\right]\zeta - \left(1/\tau_{h_a}\tau_{h_b}\right)z + \left(1/\tau_{h_a}\tau_{h_b}\right)h_{W_c} + (\bar{q}S/m)\Delta C_{L_{W_y}}(y - \bar{y}) - \left(1/\tau_{h_a}\tau_{h_b}\right)h_{L_c} \tag{49}$$

where the vertical separation $z = h_W - h_L$ and the wing and lead aircraft are assumed to have the same vertical dynamics.

The six states are x, y, ψ_W, V_W, z, and ζ. The three control inputs to the respective wing's heading-hold, Mach-hold, and altitude-hold autopilot channels are ψ_{W_C}, V_{W_C}, and h_{W_C}, respectively. The lead's control inputs are viewed as a disturbance; thus, the disturbance signals are ψ_L, V_L, and h_{L_c}. This is the full nonlinear model that is used in the simulation. For the purpose of controller design, linearization of the preceding nonlinear system yields the linear perturbation equations

$$\dot{x} = -(\bar{y}/\tau_{\psi_W})\psi_W - V_W + V_L + (\bar{y}/\tau_{\psi_W})\psi_{W_c} + \bar{y}(\bar{q}S/mV_W)\left[\Delta C_{Y_{W_y}}y + \Delta C_{Y_{W_z}}z\right] \tag{50}$$

$$\dot{y} = [(\bar{x}/\tau_{\psi_W}) - \bar{V})]\psi_W + \bar{V}\psi_L - (\bar{x}/\tau_{\psi_W})\psi_{W_c} - \bar{x}(\bar{q}S/mV_W)\left[\Delta C_{Y_{W_y}}y + \Delta C_{Y_{W_z}}z\right] \tag{51}$$

$$\dot{V}_W = -(1/\tau_V)V_W + (1/\tau_V)V_{W_c} + (\bar{q}S/m)\Delta C_{D_{W_y}}y \tag{52}$$

$$\dot{\psi}_W = (1/\tau_{\psi_W})\psi_W + (1/\tau_{\psi_W})\psi_{W_c}(\bar{q}S/mV)\left[\Delta C_{Y_{W_y}}y + \Delta C_{Y_{W_z}}z\right] \tag{53}$$

$$\dot{z} = \zeta \tag{54}$$

$$\dot{\zeta} = -\left[\left(1/\tau_{h_a}\right) + \left(1/\tau_{h_b}\right)\right]\zeta - \left(1/\tau_{h_a}\tau_{h_b}\right)z + \left(1/\tau_{h_a}\tau_{h_b}\right)h_{W_c} + (\bar{q}S/m)\Delta C_{L_{W_y}}y - \left(1/\tau_{h_a}\tau_{h_b}\right)h_{L_c} \tag{55}$$

The resulting linear state-space representation based on the defined states, controls, and disturbances is

$$\frac{\mathrm{d}}{\mathrm{d}t}\begin{bmatrix} x \\ V_W \\ y \\ \psi_W \\ z \\ \zeta \end{bmatrix} = A\begin{bmatrix} x \\ V_W \\ y \\ \psi_W \\ z \\ \zeta \end{bmatrix} + B\begin{bmatrix} V_{W_c} \\ \psi_{W_c} \\ h_{W_c} \end{bmatrix} + \Gamma\begin{bmatrix} V_L \\ \psi_L \\ h_{L_c} \end{bmatrix} \tag{56}$$

where the dynamics matrix is

$$A = \begin{bmatrix} 0 & -1 & \vdots & (\bar{q}S/mV)\Delta C_{Y_{W_y}}\bar{y} & -(\bar{y}/\tau_{\psi_W})G & (\bar{q}S/mV)\Delta C_{Y_{W_z}}\bar{y} & 0 \\ 0 & -(1/\tau_{V_W}) & \vdots & (\bar{q}S/m)\Delta C_{D_{W_y}} & 0 & 0 & 0 \\ \cdots & \cdots & \cdots & \cdots & \cdots & \cdots & \cdots \\ 0 & 0 & \vdots & (\bar{q}S/mV)\Delta C_{Y_{W_y}}\bar{x} & \left(\bar{x}/\tau_{\psi_W} - \bar{V}_L\right)G & -(\bar{q}S/mV)\Delta C_{Y_{W_z}}\bar{x} & 0 \\ 0 & 0 & \vdots & (\bar{q}S/mV)\Delta C_{Y_{W_y}}1/G & -(1/\tau_{\psi_V}) & (\bar{q}S/mV)\Delta C_{Y_{W_z}}1/G & 0 \\ 0 & 0 & \vdots & 0 & 0 & 0 & 1 \\ 0 & 0 & \vdots & (\bar{q}S/m)\Delta C_{L_{W_y}} & 0 & -\left(1/\tau_{h_a}\tau_{h_b}\right) & -\left(1/\tau_{h_a} + 1/\tau_{h_b}\right) \end{bmatrix} \tag{57}$$

the input matrix is

$$B = \begin{bmatrix} 0 & \vdots & (\bar{y}/\tau_{\psi_W})G & 0 \\ 1/\tau_{V_W} & \vdots & 0 & 0 \\ \cdots & \vdots & \cdots & \cdots \\ 0 & \vdots & -(\bar{x}/\tau_{\psi_W})G & 0 \\ 0 & \vdots & 1/\tau_{\psi_W} & 0 \\ 0 & \vdots & 0 & 0 \\ 0 & \vdots & 0 & 1/\tau_{h_a}\tau_{h_b} \end{bmatrix} \tag{58}$$

and the disturbance matrix is

$$\Gamma = \begin{bmatrix} 1 & 0 & 0 \\ 0 & 0 & 0 \\ 0 & \bar{V}_L G & 0 \\ 0 & 0 & 0 \\ 0 & 0 & 0 \\ 0 & 0 & -1/\tau_{h_a}\tau_{h_b} \end{bmatrix} \tag{59}$$

and where the number $G = \pi/180$.

VII. Control Design

Similar to the large formation control system, note that the y and z channels, viz., the states y, ψ_W, z, and ζ, are decoupled from the x channel states, x and V_W. Hence, first a controller is designed for the y and z channels, where the control signals are ψ_{W_c} and h_{W_c}. Then the design of the x-channel controller control law is

synthesized for the V_{W_c} control signal. Furthermore, even though the (y, z) model does not further decompose into individual y and z channels as in Ref. 3, where the coupling is exclusively induced by the kinematics of the large FFCS, the same controller is applied to the tight FFCS because the tight formation-induced aerodynamic coupling is rather weak.

The controller for the x and y channels contains a linear mixer on the x and y error signals and proportional plus integral action. Thus, a generalized y-channel scalar error signal is introduced, so that the lateral error and the heading error are mixed according to

$$e_y = k_y y + k_\psi e_\psi \tag{60}$$

and a linear proportional–integral (PI) control law[11] for the y channel is implemented:

$$\psi_{W_c} = K_{y_P} e_y + K_{y_I} \int_0^t e_y \, \mathrm{d}t \tag{61}$$

Similarly, in the x channel, the generalized error signal is

$$e_x = k_x y + k_V e_V \tag{62}$$

and a linear PI control law is implemented:

$$V_{W_c} = K_{x_P} e_x + K_{x_I} \int_0^t e_x \, \mathrm{d}t \tag{63}$$

The z channel controller is a standard PI controller driven by the altitude error z. The PI control law for the vertical channel is

$$h_{W_c} = K_{z_P} z + K_{z_I} \int_0^t z \, \mathrm{d}t \tag{64}$$

Building on the previous work in Refs. 2–9, the controller's gains are adjusted to achieve the desired multivariable tracking performance: In other words, the formation's geometry is maintained despite the lead's maneuvers.

VIII. Performance Evaluation

Simulations are performed for tight formations consisting of two F-16 class aircraft. The F-16 class aircraft model includes the flight control system/autopilot models, and the new tight formation stability derivatives derived earlier. The FFCS is shown in Fig. 8 and is simulated in MATLAB's SIMULINK package by The MathWorks, Inc. The tight formation's geometry is specified by $\bar{x} = 60$ ft and $\bar{y} = 23.562$ ft, or $2b$ and $(\pi/4)b$, respectively, which corresponds to minimum formation drag. Typical F-16 class aircraft data required for this work is listed in Table 1, and the evaluated tight formation stability derivatives based on this data are listed in Table 2.

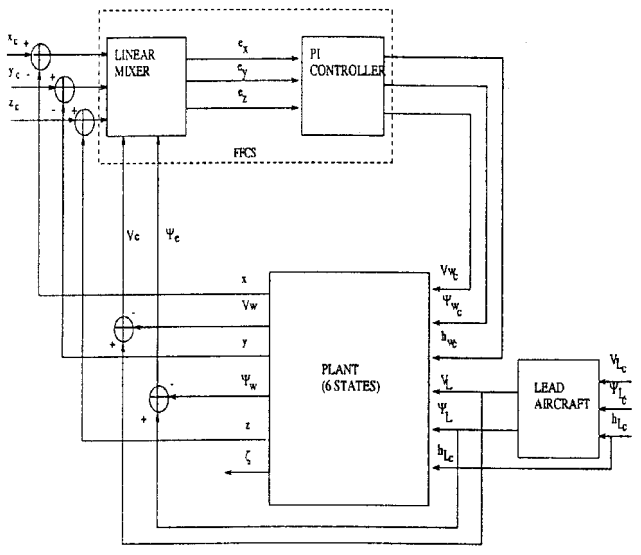

Fig. 8 FFCS.

Table 1 F-16 class aircraft characteristic values[a]

Parameter	Value
Wing area, S, ft^2	300
Wing span, b, ft	30
Aspect ratio, AR	3
Lift curve slope, a, per rad	5.3
Tail area, S_{vt}, ft^2	54.75
Tail height, h_z, in.	120
Tail lift curve slope, a_{vt}, per rad	5.3
Aerodynamic efficiency factor, η	0.95
Velocity time constant, τ_{V_W}, s	5
Heading time constant, τ_{ψ_W}, s	0.75
Altitude time constant, h_a, s	0.3075
Altitude time constant, h_b, s	3.85
Gross weight, w, lb	25,000
Gross mass, m, slugs	776.4
Velocity, $\bar{V}$, Mach ft/s	0.85 (825)

[a] Altitude of 45,000 ft and dynamic pressure 155.8 lb/ft^2.

Table 2 Tight formation stability derivatives at $\bar{y} = (\pi/4)b$ and $\bar{z} = 0$

Derivative	Value
$\Delta C_{D_{W_y}}$	−0.000782
$\Delta C_{L_{W_y}}$	−0.0077
$\Delta C_{Y_{W_y}}$	0.0033
$\Delta C_{Y_{W_z}}$	−0.0011

The dynamic A matrix evaluated for the data listed in Table 1 and the nominal $\bar{x}$, $\bar{y}$, and $\bar{z}$ separations just listed, with no tight formation-induced aerodynamic coupling effects, is

$$A = \left[\begin{array}{cc:c:cc:cc} 0 & -1.0000 & 0 & -1.2337 & & 0 & 0 \\ 0 & -0.2000 & 0 & 0 & & 0 & 0 \\ \cdots & \cdots & \cdots & \cdots & \cdots & \cdots & \cdots \\ 0 & 0 & 0 & -11.2474 & & 0 & 0 \\ 0 & 0 & 0 & -3.0000 & & 0 & 0 \\ \cdots & \cdots & \cdots & \cdots & \cdots & \cdots & \cdots \\ 0 & 0 & 0 & 0 & & 0 & 1.0000 \\ 0 & 0 & 0 & 0 & & -0.8447 & -3.5118 \end{array}\right] \tag{65}$$

The dynamics A matrix evaluated for the data listed in Table 1 and the nominal $\bar{x}$, $\bar{y}$, and $\bar{z}$ separations with the tight formation coupling effects included, is

$$A = \left[\begin{array}{cc:c:ccc} 0 & -1.0000 & 0.0057 & -1.2337 & -0.0020 & 0 \\ 0 & -0.2000 & -0.0471 & 0 & 0 & 0 \\ \cdots & \cdots & \cdots & \cdots & \cdots & \cdots \\ 0 & 0 & -0.0144 & -11.2574 & 0.0050 & 0 \\ 0 & 0 & 0.0138 & -3.0000 & 0.0138 & 0 \\ 0 & 0 & 0 & 0 & 0 & 1.0000 \\ 0 & 0 & 0.4663 & 0 & -0.8447 & -3.5118 \end{array}\right] \tag{66}$$

It can be seen from a comparison of Eqs. (65) and (66) that the aerodynamic coupling terms introduced by the tight formation are small; one notable exception is $A_{6,3} = 0.4663$, which causes the y channel to be coupled into the z channel. The y and z channels

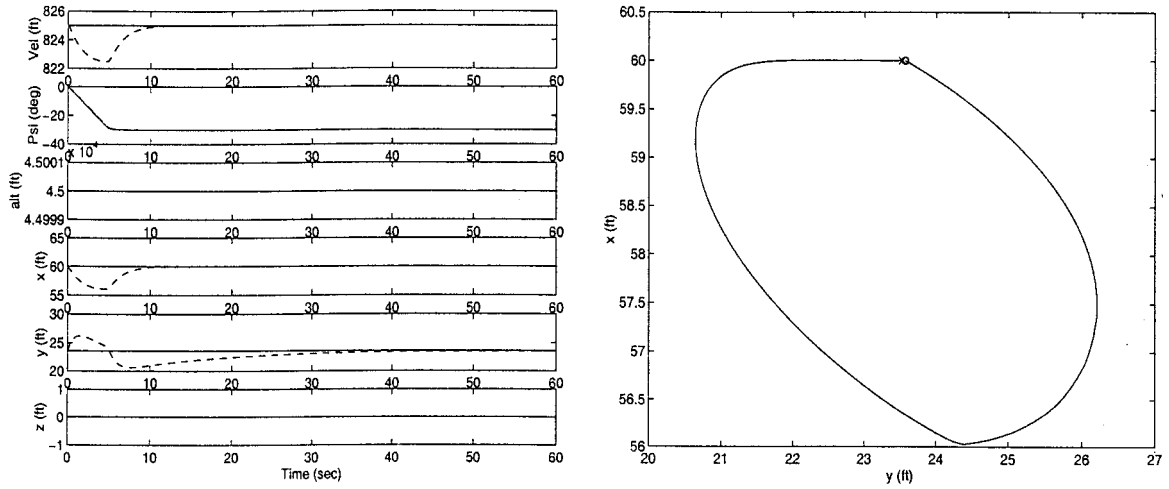

Fig. 9 Lead and wing responses for a 30-deg heading change, with no tight formation coupling effects: left, time response and right, Lissajous plot.

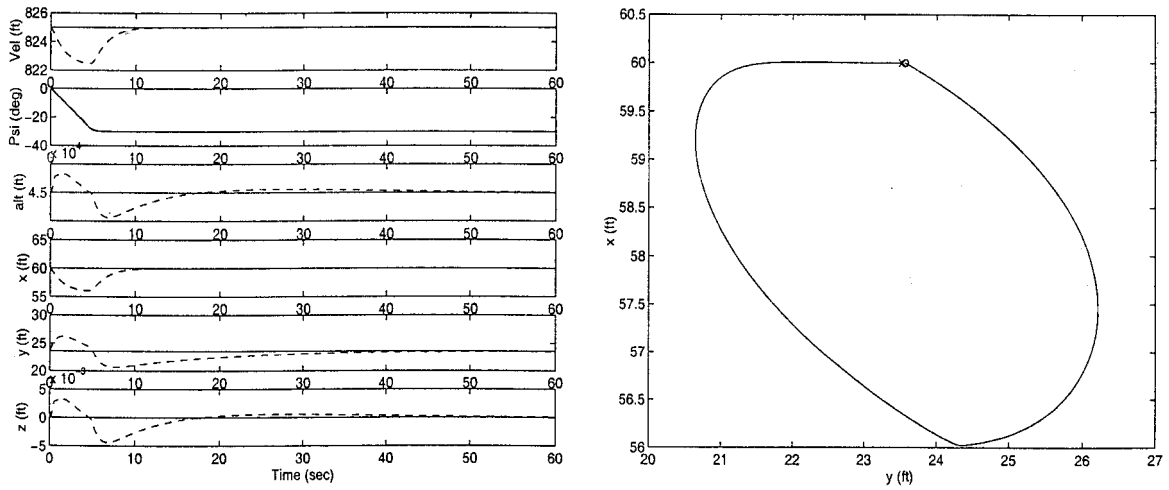

Fig. 10 Lead and wing responses for a 30-deg heading change, with tight formation coupling effects included: left, time response and right, Lissajous plot.

are still decoupled from the x channel. This justifies the use of the large formation controller because this is essentially a three-channel system, although special care is required in the z-channel controller design.

Simulations are performed in which the lead aircraft is commanded to perform a heading change of 30 deg, and the lead aircraft turns into the wing aircraft. Figure 9 shows the time response and Lissajous plots for the linearized system for a -30-deg heading change, with no tight formation aerodynamic coupling effects included. Figure 10 is the time response and Lissajous plots for the -30-deg heading change with tight formation coupling effects. The solid curves represent the lead aircraft and the dashed line represents the wing aircraft in the top three subplots. The solid line represents the nominal values in the bottom three subplots and the dashed line represents the actual values. This format is used for all time plots. The starting point in the Lissajous plots is represented by an O and the end point is represented by an X. Obviously, the formation-hold autopilot guarantees that the points O and X coincide, and, moreover, this is the only point on the Lissajous trajectory where the latter is not continuously differentiable.

The most obvious and most interesting difference between the large and tight formation time responses is the effect on the z channel of the tight formation induced coupling. This is to be expected from a comparison of Eqs. (65) and (66). The effects of the disturbances are unnoticeable on the horizontal channels, as expected, bearing in mind the small numerical values of the tight formation dynamics' new stability derivatives. The closest the aircraft come to one another is $1\frac{6}{7}b$ in the x direction and $\frac{2}{3}b$ in the y direction during the 30-deg heading change maneuver, viz., the x and y deviations peak at $\frac{1}{7}b = 0.14b$ and $(\pi/4 - \frac{2}{3})b = 0.11b$, respectively. The x-channel transient settles within 20 s and the y channel settles within 60 s. The gains have been chosen to produce approximately equal maximum positive and negative perturbations from the optimal position. This can be seen in Fig. 9 in which the deviation to the right is approximately equal to the deviation to the left. The second criterion for gain selection was to maintain a consistent response for both a positive and a negative change in either the heading or the velocity. The third criterion for selecting the gains was to keep the wing from crossing over either axis. The third criterion has the dual effect of preventing a collision between the lead and the wing; also, a collision is prevented in a formation containing both a left and a right wing aircraft. The gains for the vertical channel were also chosen based on the first two criteria identified for the horizontal channel. The gain values are listed in Table 3. During the maneuvers, formation spacing is maintained within 14% of the wingspan in both the $\hat{x}$ and $\hat{y}$ directions, and there is a negligible change in the $\hat{z}$ direction. Zero steady-state tracking errors are recorded after the cross coupled tight formation heading change is complete. Therefore, the large FFCS (designed such that only the kinematic coupling effects are acknowledged when the aerodynamic coupling effects are neglected) can handle the aerodynamic coupling effects created by a lead aircraft's wings in a tight formation and maintains the formation. Furthermore, the FFCS can maintain the formation spacing within the required $10\%b$ tolerance for the following lead manuevers: a lead heading change of ± 20 deg, a lead velocity change of ± 50 ft/s, and a lead altitude change of ± 400 ft (Ref. 10). Most

Table 3 FFCS gains

FFCS gains	Numerical value
Linear mixer	
k_V	12.5
k_ψ	6.0
k_x, s^{-1}	−8.0
k_y, deg/ft	−0.6
k_z	25.0
PI compensator	
K_{X_P}	6.0
K_{X_I}	0.4
K_{Y_P}	11.0
K_{Y_I}	0.9
K_{Z_P}	4.0
K_{Z_I}	0.5

importantly, within this operational envelope, autopilot saturation effects, extensively investigated in Refs. 2–10 play a role. This was borne out during simulations performed on the nonlinear model which included saturation effects, as documented in Ref. 10.

IX. Conclusions

The tight formation aerodynamic coupling effects on the wing aircraft caused by the lead's wing vortex have been included in the formation control system's dynamics. A tight formation control system for the wing aircraft is designed. It is shown that a formation control system designed without due consideration of the aerodynamic coupling effects caused by a tight formation configuration and where only the kinematic coupling effects are accounted for can handle the additional aerodynamic coupling effects caused by tight formation flying. The automatic formation flight controller can maintain the formation geometry within the required 10%b tolerance in the face of lead maneuvers, provided that the lead heading change is not more then ±20 deg, a lead velocity change of ±50 ft/s, and a lead altitude change of ±400 ft. Thus, the developed tight formation flight controller can enable aircraft to take advantage of the reduction in induced drag brought about by the aerodynamic coupling effects. This will reduce the formation's fuel consumption and extend formation range and endurance. The novel FFCS will also enable multiple unihabited air vehicles to fly together in a controlled tight formation during surveillance missions.

References

[1]Blake, W., and Multhopp, D., "Design, Performance and Modeling Considerations For Close Formation Flight," *AIAA Guidance, Navigation, and Control Conference*, AIAA, Reston, VA, July 1998.

[2]Dargan, J., Pachter, M., and D'Azzo, J. J., "Automatic Formation Flight Control," *AIAA Guidance, Navigation, and Control Conference*, AIAA, Washington, DC, 1992, pp. 838–857.

[3]Pachter, M., D'Azzo, J. J., and Dargan, J. L., "Automatic Formation Flight Control," *Journal of Guidance, Control, and Dynamics*, Vol. 17, No. 6, 1994.

[4]Pachter, M., D'Azzo, J. J., and Buzogany, L., "Automated Control of Aircraft in Formation Flight," *AIAA Guidance, Navigation, and Control Conference*, AIAA, Washington, DC, 1993, pp. 1349–1370.

[5]Pachter, M., D'Azzo, J. J., and Reyna, V., "Automation of Formation Flight Control," *AIAA Guidance, Navigation, and Control Conference*, AIAA, Washington, DC, 1994, pp. 1379–1404.

[6]Veth, M., Pachter, M., and D'Azzo, J. J., "Autopilots for Flying Circular Paths," *AIAA Guidance, Navigation, and Control Conference*, AIAA, Washington, DC, 1995, pp. 1446–1458.

[7]Pachter, M., D'Azzo, J. J., and Veth, M., "Energy Preserving Formation Flight Control," AIAA Paper 95-0335, 1995.

[8]McCammish, S., Pachter, M., and D'Azzo, J. J., "Optimal Formation Flight Control," AIAA Paper 96-3868, July 1996.

[9]Pachter, M., D'Azzo, J. J., and Veth, M., "Proportional and Integral Control of Non-Linear Systems," *International Journal of Control*, Vol. 64 No. 4, 1996, pp. 679–692.

[10]Blakelock, J. H., *Automatic Control of Aircraft and Missiles*, 2nd ed., Wiley, New York, 1991.

[11]D'Azzo, J. J., and Houpis, C. H., *Linear Control System Analysis and Design*, 4th ed., McGraw–Hill, New York, 1995.